Chinese Chemical Letters 36 (2025) 110062

Contents lists available at ScienceDirect

Chinese Chemical Letters

journal homepage: www.elsevier.com/locate/cclet

Facile construction of $Cu_{2-x}Se$@C nanobelts as anode for superior sodium-ion storage

Yanxue Wu[a], Xijun Xu[b,d,*], Shanshan Shi[c], Fangkun Li[e], Shaomin Ji[b,d], Jingwei Zhao[f], Jun Liu[e,*], Yanping Huo[a,b,d,*]

[a] Analysis and Test Center, Guangdong University of Technology, Guangzhou 510006, China
[b] Guangdong Provincial Laboratory of Chemistry and Fine Chemical Engineering Jieyang Center, Jieyang 515200, China
[c] R& D Center, Yunnan Yuntianhua Co., Ltd., Kunming 650228, China
[d] School of Chemical Engineering and Light Industry, Guangdong University of Technology, Guangzhou 510006, China
[e] Guangdong Provincial Key Laboratory of Advanced Energy Storage Materials, School of Materials Science and Engineering, South China University of Technology, Guangzhou 510641, China
[f] Research and Development Center, Guangzhou Tinci Materials Technology Co., Ltd., Guangzhou 510765, China

ARTICLE INFO

Article history:
Received 30 April 2024
Accepted 27 May 2024
Available online 28 May 2024

Keywords:
$Cu_{2-x}Se$@C
Nanobelts
Metal-organic framework (MOF)
Anode
Sodium-ion batteries

ABSTRACT

Transition metal selenides are considered promising electrochemical energy storage materials due to their excellent rate properties and high capacity based on multi-step conversion reactions. However, its practical applications are hampered by poor conductivity and large volume variation for Na^+ storage, which resulting fast capacity decay. Herein, a facile metal-organic framework (MOF) derived method is explored to embed $Cu_{2-x}Se$@C particles into a carbon nanobelts matrix. Such carbon encapsulated nanobelts' structural moderate integral electronic conductivity and maintained the structure from collapsing during Na^+ insertion/extraction. Furthermore, the porous structure of these nanobelts endows enough void space to mitigate volume stress and provide more diffusion channels for Na^+/electrons transporting. Due to the unique structure, these $Cu_{2-x}Se$@C nanobelts achieved ultra-stable cycling performance (170.7 mAh/g at 1.0 A/g after 1000 cycles) and superior rate capability (94.6 mAh/g at 8 A/g) for sodium-ion batteries. The kinetic analysis reveals that these $Cu_{2-x}Se$@C nanobelts with considerable pesoudecapactive contribution benefit the rapid sodiation/desodiation. This rational design strategy broadens an avenue for the development of metal selenide materials for energy storage devices.

The current society witnesses a rapid surge in electronic products aggravating the global energy demand, also bringing great pressure to the ecological environment [1-7]. There is an urgent need to develop new types of energy to replace traditional fossil energy. Clean energy, such as wind, solar, and tidal energy are all intermittent, resulting in a great demand for energy storage and conversion equipment. Lithium-ion batteries (LIBs) have been poured into our daily lives due to their high output voltage and energy density [8-15]. However, its further wide application is severely impeded by the limited lithium salt and expensive cost. Sodium-ion batteries (SIBs) have similar operating principles to LIBs and have emerged as a promising alternative to partially replace LIBs. Despite slightly lower energy density, the widely distributed sodium salts with abundant preserves are cheap, which is beneficial for large energy storage systems [16-18]. Nevertheless, the ionic radius of Na^+ (1.02 Å) is much larger than that of Li^+ (0.76 Å), causing requires for electrodes more strict can't be inherited from LIBs' materials [19,20]. Especially for anode materials, Na^+ can't form the intercalated compound with graphite making them unsuitable for SIBs [21-23].

So, it is still a challenge to design materials with interstitial volumes and open frameworks for the accommodation of Na^+ insertion/extraction [20,22]. Up to now, various anode materials have been explored, such as transition metal oxides [24,25], sulfides [26,27], selenides [28-31], phosphates [32,33], organic compounds [34,35]. Among them, transition metal selenides (TMSs) have relatively small polarization and relatively higher electrical conductivity than oxides [25,36]; Metal sulfide has polysulfur ion dissolution in the electrochemical cycle, resulting in poor cycle and multiplier performance, while TMSs can effectively avoid the reaction in the cycle process [27,37]. Meanwhile, selenium atoms with larger diameters and are more metallic than sulfur atoms, thus

* Corresponding authors.
E-mail addresses: xuxijun2022@gdut.edu.cn (X. Xu), msjliu@scut.edu.cn (J. Liu), yphuo@gdut.edu.cn (Y. Huo).

https://doi.org/10.1016/j.cclet.2024.110062
1001-8417/

metal selenide has larger layer spacing and higher conductivity than metal sulfide [38,39]. However, the conductivity of TMSs still cannot meet the requirements of high-rate charging/discharging, and there is still a certain volume change in the process of Na^+ insertion/extraction, leading to the structural change of the electrode material and the instability of the solid electrolyte interface (SEI) film, resulting limited electrochemical performance [40-42]. Therefore, it is still necessary to further modify these TMSs to achieve superior Na-ion storage. To address the above problems, many strategies have been explored to improve Na^+ diffusion kinetic and enhance the interface stability [42-44]. For example, Liu *et al.* fabricated the unique Fe_7Se_8@C nanotubes *via* a facile template-based method and delivered a maintainable capacity of 222 mAh/g over 500 cycles at 2 A/g [45]. Lou *et al.* constructed hierarchical microboxes composed of Cu-doped $CoSe_2$ ultrathin nanosheets *via* a template-engaged strategy and obtained a high capacity retention of 94% over 500 cycles at 1.0 A/g [46]. Song *et al.* successfully synthesized a carbon-regulated Cu_2Se@C by selenidation of Cu_2O and then carbon coating, this anode achieved excellent Li^+ storage performance with a capacity retention of 83% after 1500 cyles at 5.0 A/g [47]. Apparently, the Na^+ storage performance of these selenides has been dramatically improved through nanostructural designing and surface modification [48-50]. Among these selenides, $Cu_{2-x}Se$ exhibits excellent electrical conductivity due to the Cu ions are in a superionic state, and Se atoms are in a face-centered cubic position. In addition, the volume of $Cu_{2-x}Se$ spatial units is much larger than other copper selenides with similar crystal structures and can accommodate more Na ions for high capacity [51-54]. On account of these points, fabricating $Cu_{2-x}Se$ nanoparticles encapsulated in a carbon framework will definitely improve its electrochemical performance. Recently, metal-organic framework (MOF) derived methods have been verified as a facile strategy to *in-situ* encapsulate active nanoparticles in carbon matrix by pyrolyzation [55]. These MOF-derived carbon frameworks will dramatically enhance the electronic conductivity, ensure fast transporting of Na^+/electrons, and thus prevent the electrode structure from collapsing during Na^+ insertion/extraction.

Herein, a more convenient synthetic strategy was developed for preparing Cu-BTC nanobelts *via* continuously stirring the mixture solution of water/ethanol at room temperature, which contains copper nitrate and trimesic acid. The $Cu_{2-x}Se$@C nanobelts were obtained *via* a MOF-derived strategy coupled with a hydrothermal selenidation method. The $Cu_{2-x}Se$ nanoparticles encapsulated in a carbon matrix not only mitigate volume expansion but also improve electronic conductivity. As an anode for SIBs, these $Cu_{2-x}Se$@C nanobelts achieved ultra-stable cycling performance (170.7 mAh/g at 1.0 A/g after 1000 cycles) and superior rate capability (94.6 mAh/g at 8 A/g) for SIBs.

As illustrated in Fig. 1a, the Cu-BTC nanobelts were prepared *via* a facile precipitation reaction by mixing $Cu(NO_3)\cdot 3H_2O$ and trimesic acid in distilled water with continuous stirring. Then, the Cu-BTC precursor was annealed at 350 °C for 2 h under an Ar atmosphere to get Cu@C. Finally, the Cu@C was mixed with Se powder and further selenylated to obtain $Cu_{2-x}Se$@C nanobelts. Scanning electron microscopy (SEM) was performed to reveal the morphology of Cu-BTC and $Cu_{2-x}Se$@C (Figs. 1b–g). As displayed in Figs. 1b–d, the Cu-MOF has a smooth and neat nanobelts structure with a width of ~200 nm and a length of tens of microns. It is evident that the surface of the nanobelts becomes rough through pyrolyzation and after selenidation (Figs. 1e–g). Fortunately, the final product (Figs. 1e–g) preserved the nanobelts' shape, and all the Cu_2Se nanoparticles were wrapped on nanobelts.

The phase information of intermediate Cu@C and final Cu_2Se@C nanobelts were verified by X-ray diffraction (XRD). Fig. S1a (Supporting information) exhibits the XRD pattern of the Cu@C, which

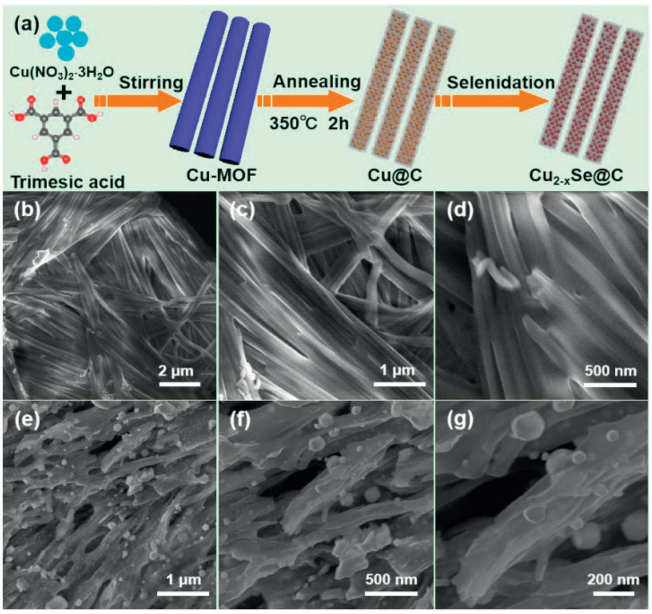

Fig. 1. (a) Schematic illustration for the fabrication of $Cu_{2-x}Se$@C nanobelts. (b-d) SEM images of Cu-MOF nanobelts (e-g) SEM images of Cu_2Se@C nanobelts.

clearly shows three main peaks of (111), (200), and (320) well matched with the standard PDF card (JCPDS card No. 65-7737). It is proved that the Cu-MOF after pyrolyzation at 350 °C for 2 h obtained Cu@C. The XRD pattern of $Cu_{2-x}Se$@C (Fig. 2a) exhibit diffraction peaks at 26.75°, 31.03°, 44.60°, 52.91°, 64.98°, and 71.59° can be assigned to the (111), (200), (220), (311), (400) and (331) crystal plane of cubic $Cu_{2-x}Se$ (JCPDS card No. 65-2982), respectively. It is demonstrated that the $Cu_{2-x}Se$ nanobelts were successfully prepared *via* a facile MOF-derived strategy folowed by the hydrothermal selenidation method.

The carbon content of $Cu_{2-x}Se$@C was measured by thermogravimetric analysis (TGA), which is carried out in the air condition and the results are displayed in Fig. S2 (Supporting information). The initial weight loss in the region of 150–500 °C is attributed to the evaporation of absorbed water. The obvious weight loss of 56.83% that occurred in the region of 150–750 °C is ascribed to the $Cu_{2-x}Se$@C oxidized to CuO, SeO_2, CO_2, and the sublimation of SeO_2 [54,55]. Based on the final product (CuO) of $Cu_{2-x}Se$@C heating from 40 °C to 750 °C under air atmosphere, it could be concluded the $Cu_{2-x}Se$ in these composites is about 60.02 wt%. The results are well match the energy-dispersive X-ray spectra result (Fig. S3 in Supporting information). The physical adsorption method was used to explore the specific surface area and pore size distribution of $Cu_{2-x}Se$@C nanobelts (Figs. 2b and c). The adsorption-desorption isotherms of $Cu_{2-x}Se$@C nanobelts were typical type IV isotherms. According to the Brunauer-Emmett-Teller (BET) results, the surface area and average pore size are calculated to be around 190.22 m^2/g and 1.08 nm, respectively. Moreover, the Barrett-Joyner-Halenda results show that the pore volume $Cu_{2-x}Se$@C is 0.068 cm^3/g. The chemical composition and valence state of $Cu_{2-x}Se$@C was analyzed by X-ray photoelectron spectroscopy (XPS). As recorded in Fig. 2d, the high-resolution Cu 2p spectra of $Cu_{2-x}Se$@C nanobelts are annotated two doublets, corresponding to $2p_{1/2}$ at 949.4 eV and $2p_{3/2}$ at 929.4 eV of Cu^+ as well as $2p_{1/2}$ at 951.4 eV and $2p_{3/2}$ at 931.3 eV of Cu^{2+}, respectively [56,57]. The peaks located at 959.9 eV and 939.6 eV are attributed to the satellite peaks of Cu 2p. After analyzing the spectrum of Se 3d in Fig. 2e, the two peaks located at 51.4 eV and 52.9 eV are corresponding to Se $3d_{5/2}$ and Se $3d_{5/2}$, respectively, which are attributed to the Se^{2-} in $Cu_{2-x}Se$@C [54,56,57]. The peak at 53.7 eV and weak peak at 55.9 eV were associated

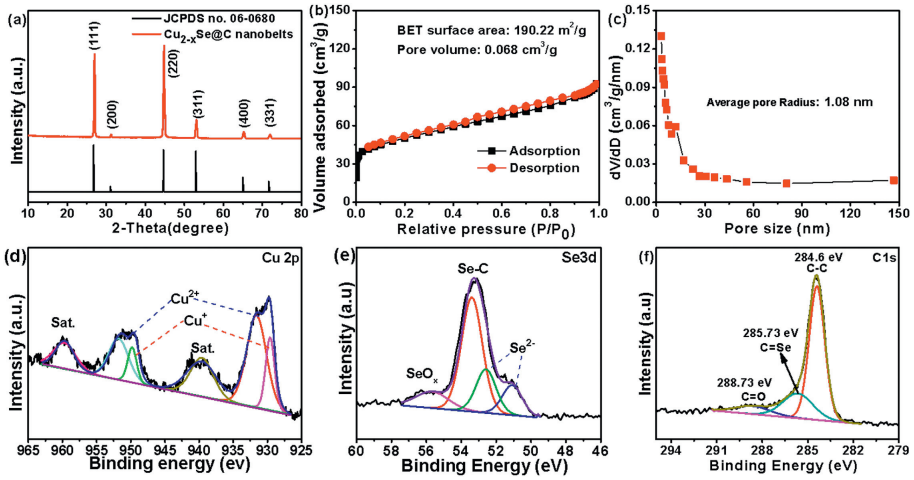

Fig. 2. (a) XRD patterns of $Cu_{2-x}Se$@C. (b) Nitrogen adsorption-desorption isotherms of $Cu_{2-x}Se$@C. (c) The corresponding pore size distribution for $Cu_{2-x}Se$@C. XPS spectra of the $Cu_{2-x}Se$@C (d) Cu 2p, (e) Se 3d, and (f) C 1s.

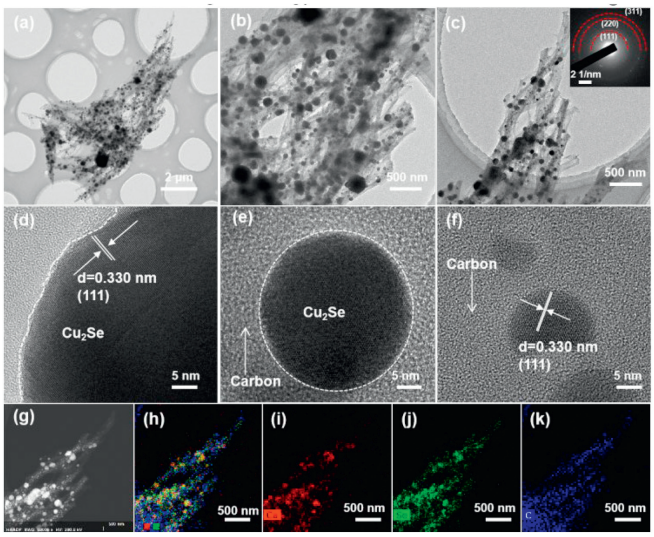

Fig. 3. (a-c) TEM images of $Cu_{2-x}Se$@C nanobelts. (d) SAED pattern of $Cu_{2-x}Se$@C nanobelts. (e, f) HRTEM images of $Cu_{2-x}Se$@C nanobelts. (g-k) EDS mapping images of $Cu_{2-x}Se$@C nanobelts.

with the Se-C and SeO_x bond in $Cu_{2-x}Se$@C nanobelts, respectively. In the spectrum of C 1s (Fig. 2f), the peaks with binding energies of 288.73, 285.73, and 284.6 eV belonged to C=O, C=Se, and C–C bonds, respectively [56,57]. Based on the above analysis, it is proved that the prepared nanobelts material is $Cu_{2-x}Se$@C. These $Cu_{2-x}Se$@C nanobelts with a high surface area could form good contact with electrolytes and provide more channels for Na^+, thus promising a superior electrochemical performance for SIBs.

The microstructure features of $Cu_{2-x}Se$@C were further revealed by transmission electron microscopy (TEM) and high-resolution TEM (HRTEM). As displayed in Figs. 3a–c, $Cu_{2-x}Se$@C demonstrates a clear nanobelt shape and the size is well according to the SEM results. It can be observed that the tiny $Cu_{2-x}Se$ nanoparticles are fully embedded in the carbon nanobelts. The insert select area electron diffraction (SAED) in Fig. 3c exhibits three obvious diffraction rings are belong to (111), (220), and (331) planes of cubic $Cu_{2-x}Se$, respectively. The HRTEM image (Figs. 3d–f) reveals the nanoparticle with an interplanar crystal length of 0.330 nm, which can be indexed to the (111) crystal plane of $Cu_{2-x}Se$. The HRTEM image in Fig. 3e exhibits the $Cu_{2-x}Se$@C with a size of ~30 nm well encapsulated by amorphous carbon. From the TEM results, can be concluded that the size of $Cu_{2-x}Se$ nanoparticles is from tens to hundreds of nanometers. Furthermore, the corresponding elemental mapping signals were also collected (Figs. 3g–k), evidently revealing a uniform distribution of Cu, Se, and C elements. The signals of Cu and Se elements are well overlapped and confined in the C element signal, emerging as a nanobelts-shape. The TEM results indicating the final products inherit the nanobelts shape of Cu-MOF and the rational design strategy is feasible to obtain $Cu_{2-x}Se$@C nanobelts.

To evaluate the Na^+ storage performance of these $Cu_{2-x}Se$@C nanobelts, coin-type (CR2025) $Cu_{2-x}Se$@C//Na half cells were assembled, and galvanostatic discharge/charge and cyclic voltammetry were carried out. Unveiled from Fig. 4a, a distinct peak located at 0.88 V in the initial cathodic scan and vanishes in the following cycles, which indicates that the Cu_2Se@C anode experiences multiple electrochemical reactions and irreversible formation of solid electrolyte interphase (SEI) layer [54,55]. The current peaks at 1.95 V and 1.62 V correspond to intercalation of Na^+ into Cu_2Se form Na_xCuSe, and further sodiation to NaCuSe phases at 1.28 V [44,45]. Furthermore, the cathodic peak at 0.68 V is associated with a conversion reaction from NaCuSe to metallic Cu and Na_2Se. During the anodic scan, the peak of about 1.52 V is related to the reversible conversion reaction of Na_2Se and Cu to NaCuSe, and another weakened one at 2.04 V results from the formation of Cu_2Se phase [57,58]. The subsequent CV profiles of Cu_2Se@C nearly overlap with the second cycle, demonstrating its high reversibility with Na and outstanding cycling stability. Fig. 4b delineates the galvanostatic discharge/charge curves of $Cu_{2-x}Se$@C nanobelts, where the first discharge/charge capacities are 274.1 and 215.4 mAh/g, respectively. The corresponding initial Coulombic efficiency (ICE) is about 79.26%, which is associated with the irreversible formation of the SEI layer. Furthermore, the discharge/charge curves exhibit a similar potential platform from 10 cycles to 200 cycles, demonstrating the great cycling stability of $Cu_{2-x}Se$@C nanobelts. To further evaluate the Na^+ ion storage performance of $Cu_{2-x}Se$@C nanobelts, voltage-capacity profiles at various current densities were carried out and depicted in Fig. 4c. There is almost no polarization below 2.0 A/g suggesting this porous nanobelts structure endows $Cu_{2-x}Se$@C superior diffusion ability of Na^+/electrons. As depicted in Fig. 4d, $Cu_{2-x}Se$@C anode achieved average capacities of 253.2, 235.2, 213.6, 198.8, 181.4, 147.3 and 94.6 mAh/g at 0.1, 0.2, 0.5, 1.0, 2.0, 4.0, and 8.0 A/g, respectively. With the current density returned to 0.1 A/g, $Cu_{2-x}Se$@C nanobelts can regain a reversible capacity of 264.0 mAh/g, demonstrating its impressive rate performance. Except for the fascinating rate capacities, $Cu_{2-x}Se$@C

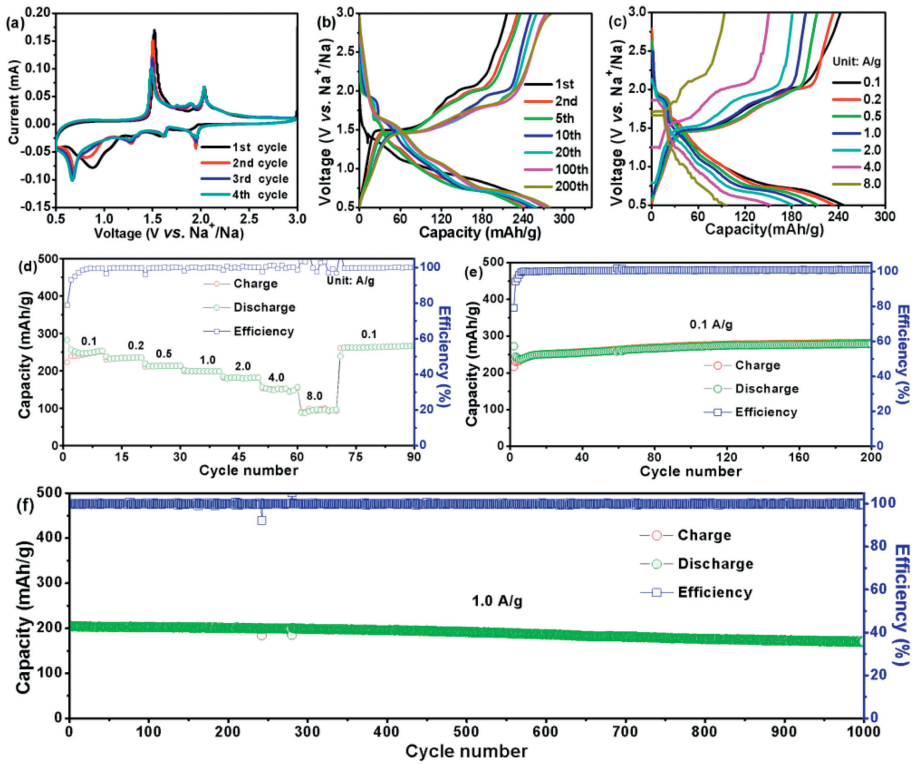

Fig. 4. (a) CV curves of $Cu_{2-x}Se$@C with a scan rate of 0.2 mV/s. (b) The selected cycled discharge–charge curves of $Cu_{2-x}Se$@C. (c) GCD profiles of Cu_2Se@C electrodes. (d) Rate capability at various current densities from 0.1 A/g to 8.0 A/g. (e) Cycle stability at 0.1 A/g. (g) Long-cycling performance of $Cu_{2-x}Se$@C at 1 A/g.

nanobelts also exhibit outstanding cycling stability. It can be observed that the $Cu_{2-x}Se$@C electrode exhibits a stable capacity of 278.6 mAh/g at 0.1 A/g after 200 cycles (Fig. 4e). Even cycled at a high current density of 1.0 A/g (Fig. 4f), this $Cu_{2-x}Se$@C nanobelts can still attain 170.7 mAh/g over 1000 cycles with CE of ~100.0%.

To investigate the detailed kinetic behaviors of the as-prepared $Cu_{2-x}Se$@C nanobelts, CV profiles were recorded under various scan rates (from 0.1 mV/s to 1.5 mV/s). As displayed in Fig. 5a, with the increase in scan rate, the corresponding current response increased. These CV curves keep similar shapes illustrating the impressive rate capability of Cu_2Se@C nanobelts.

The cathodic and anodic peaks with a little shift originate from the enhanced current polarization. Specifically, the relationship of peak current (i) *versus* scan rate (v) abides by the following Dunn's empirical formula [59,60]:

$$i = av^b \tag{1}$$

in which a and b are empirical parameters and the value can calculated through linear fitting of log(i) *versus* log(v). As is well-known, b value nearing 0.5 or 1.0 indicates a diffusion-controlled and capacitance-controlled process, respectively. As for Cu_2Se@C nanobelts, the calculated b-values of peak C1, C2, D1, D2 and D3 are 0.74, 0.87, 0.83, 0.88 and 0.86, respectively, demonstrating the Na^+ insertion/extraction process is occupied by pseudocapacitive behavior (Fig. 5b). These results might be attributed to the porous nanobelts structure, which endows more channels for Na^+ ions diffusion. Furthermore, the pseudocapacitive contribution of Cu_2Se@C nanobelts can be quantitatively distinguished. At specific potentials, the pseudocapacitive fraction (k_2v) and diffusion-controlled part ($k_1v^{1/2}$) abiding following equation [61,62]:

$$i(\mathrm{V}) = k_2v + k_1v^{1/2} \tag{2}$$

Eq. 2 can be reformulated as:

$$i(\mathrm{V})/v^{1/2} = k_1 + k_2v^{1/2} \tag{3}$$

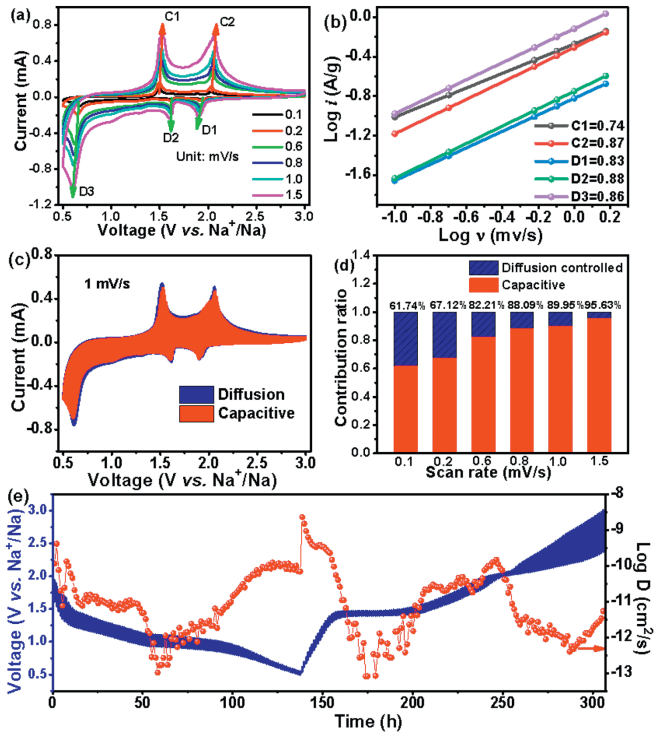

Fig. 5. (a) CV curves at various scan rates (from 0.1 mV/s to 1.5 mV/s). (b) Relationship between log(i) and log(v). (c) CV curve and capacitive contribution at 1 mV/s. (d) Capacitive contribution at different scan rates. (e) GITT profiles for $Cu_{2-x}Se$@C nanobelts at the initial discharge/charge process and the corresponding Na^+ diffusion coefficient.

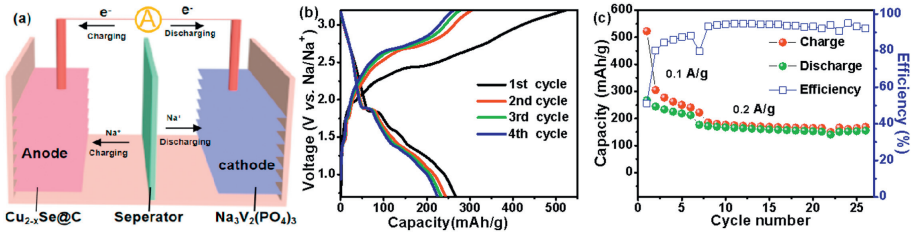

Fig. 6. (a) The schematic of $Na_3V_2(PO_4)_3$//$Cu_{2-x}Se$@C nanobelts full cell. (b) Initial four charge-discharge curves of $Na_3V_2(PO_4)_3$//$Cu_{2-x}Se$@C full cell. (c) Cycling performance of $Na_3V_2(PO_4)_3$//$Cu_{2-x}Se$@C at 0.2 A/g.

Accordingly, the k_2-value can be simply obtained by linear fitting $i(V)/v^{1/2}$ *vs.* $v^{1/2}$, and the pseudocapacitive part (k_2v) can be easily determined. As depicted in Fig. 5c, the pseudocapacitive contribution of $Cu_{2-x}Se$@C nanobelts is as high as 89.95% at 1.0 mV/s. Apparently, the $Cu_{2-x}Se$@C nanobelts anode possesses distinct pseudocapacitive contribution ratios of 61.74%, 67.12%, 82.21%, 88.09%, 89.95% and 95.63% at 0.1, 0.2, 0.6, 0.8, 1.0 mV/s to 1.5 mV/s (Fig. 5d). These results illustrating that the Na-ions storage in this $Cu_{2-x}Se$@C anode is overwhelmed by superficial and interfacial storage behaviors. The carbon played as a protective shell and porous structure are capable of alleviating the volume change, thus achieving excellent Na-ions storage performance. As shown in Fig. 5e, the calculated Na^+ diffusion coefficient has a magnitude of approximately 10^{-12} S/cm^2. The relatively smaller diffusion coefficient at the voltage platform could be ascribed to the electrochemical reaction-controlled step. The large Na^+ diffusion coefficient and robust carbon-encapsulated nanotube structure can effectively mitigate the large volume variation and keep the structure integrity of the $Cu_{2-x}Se$@C anode during the Na^+ insert/extract processes. On account of this, the morphology information after 120 cycles at 2.0 A/g was carried out by SEM measurement (Fig. S4 in Supporting information). The EIS results of $Cu_{2-x}Se$@C nanotubes (Fig. S5 in Supporting information) after cycles also confirm this rational design will promote the Na^+/ions transporting. As displayed in these images, the nanobelt structure is basically preserved, revealing that this porous framework could well protect the structure integrity from destroying during the electrochemical process.

To further investigate the electrochemical performance of $Cu_{2-x}Se$@C nanobelts, the full cell was carried out with $Na_3V_2(PO_4)_3$ as the cathode. Fig. 6a shows the schematic illustration of $Na_3V_2(PO_4)_3$//$Cu_{2-x}Se$@C nanobelts full cell. As exhibited in Fig. S6 (Supporting information), $Na_3V_2(PO_4)_3$ cathode exhibits a long charging/discharging voltage platform at 3.41 V/3.33 V, respectively. Fig. 6b depicts the first four capacity-voltage curves of $Na_3V_2(PO_4)_3$//$Cu_{2-x}Se$@C full cell with obvious discharge/charge platforms, whose locations are well consistent with the discharge/charge platforms of $Na_3V_2(PO_4)_3$ cathode and $Cu_{2-x}Se$@C anode. Substantially, $Na_3V_2(PO_4)_3$//$Cu_{2-x}Se$@C displays a capacity of 160 mAh/g (based on $Cu_{2-x}Se$@C anode) after 27 cycles at 0.2 A/g in the voltage region of 0.7~3.2V, yielding an initial coulombic efficiency of 51.2% (Fig. 6c). Furthermore, compare with previous reported Cu-based chalcogenides (Table S1 in Supporting information), this $Cu_{2-x}Se$@C nanobelts anode also shown some advantages on the specific capacity and long cycle stability. These results also reflected that the MOF-derived strategy *in situ* formed a conductive framework encapsulated the active $Cu_{2-x}Se$ nanoparticles, which not only improved the electronic conductivity but also preserved the integral structure from collapsing, thus achieving superior Na^+ storage performance.

In summary, $Cu_{2-x}Se$@C nanobelts were successfully synthesized *via* a facile MOF-derived strategy combined with a hydrthermal selenidation method. As an anode for SIBs, these $Cu_{2-x}Se$@C nanobelts achieved 278.6 mAh/g at 0.1 A/g after 200 cycles and 170.7 mAh/g at 1.0 A/g after 1000 cycles. Cycled at 0.1, 0.2, 0.5, 1.0, 2.0, 4.0, and 8.0 A/g, the $Cu_{2-x}Se$@C nanobelts attained 253.2, 235.2, 213.6, 198.8, 181.4, 147.3 and 94.6 mAh/g, respectively. The ultra-stable cycling performance and superior rate capability can be attributed to carbon encapsulated nanobelts' structural enhanced integral electronic conductivity and preserved the structure from collapsing during Na^+ insertion/extraction. Furthermore, the porous structure of these nanobelts endows enough void space to mitigate volume stress and provide more diffusion channels for Na^+/electrons transporting. The kinetic analysis reveals that these $Cu_{2-x}Se$@C nanobelts with considerable pesoudecapactive contribution benefit the rapid charge transfer. This synthesis strategy sheds light on the designing of metal selenide materials for alkali-ion batteries.

Declaration of competing interest

The authors declare that they have no known competing financial interests or personal relationships that could have appeared to influence the work reported in this paper.

CRediT authorship contribution statement

Yanxue Wu: Data curation, Writing – original draft. **Xijun Xu:** Conceptualization, Supervision, Writing – review & editing. **Shanshan Shi:** Formal analysis, Investigation. **Fangkun Li:** Investigation, Methodology. **Shaomin Ji:** Visualization. **Jingwei Zhao:** Resources. **Jun Liu:** Conceptualization, Supervision. **Yanping Huo:** Conceptualization, Resources, Supervision.

Acknowledgments

This work was supported by the National Key Research and Development Program of China (No. 2022YFB2502000), the National Natural Science Foundation of China (Nos. U21A2033251771076, 52301266, 42203047), R&D Program in Key Areas of Guangdong Province (No. 2020B0101030005), Science and Technology Planning Project of Guangzhou (No. 2024A04J9999), and GDUT Large-Scale Instruments Open Foundation (No. ATC2022201).

Supplementary materials

Supplementary material associated with this article can be found, in the online version, at doi:10.1016/j.cclet.2024.110062.

References

[1] F. Wu, J. Maier, Y. Yu, Chem. Soc. Rev. 49 (2020) 1569–1614.
[2] M. Li, J. Lu, Z. Chen, K. Amine, Adv. Mater. 30 (2018) 1800561.
[3] F. Li, Z. Liu, C. Liao, et al., ACS Energy Lett. 8 (2023) 4903–4914.
[4] Z. Zhuang, F. Zhang, D. Gandla, et al., ACS Appl. Mater. Interfaces 15 (2023) 38530–38539.
[5] V.V. Jadhav, Z. Zhuang, S.N. Banitaba, et al., Dalton Trans. 52 (2023) 14564–14572.

[6] Z. Zhuang, F. Zhang, Y. Zhou, et al., Mater. Today Energy 30 (2022) 101192.
[7] Z. Zhuang, C. Liu, Y. Yan, P. Ma, D.Q. Tan, J. Mater. Chem. A 9 (2021) 27095–27101.
[8] P.K. Nayak, L. Yang, W. Brehm, P. Adelhelm, Angew. Chem. Int. Ed. 57 (2018) 102–120.
[9] H.S. Hirsh, Y. Li, D.H. Tan, et al., Adv. Energy Mater. 10 (2020) 2001274.
[10] P. Ma, Z. Zhuang, J. Cao, B. Ju, X. Xi, ACS Appl. Energy Mater. 5 (2022) 6417–6422.
[11] Z. Zhuang, L. Yang, B. Ju, et al., Chem. Select. 5 (2020) 2291–2299.
[12] A. Yin, L. Yang, Z. Zhuang, et al., Energy Storage 2 (2020) e132.
[13] Z. Zhuang, L. Yang, B. Ju, et al., Energy Storage 2 (2020) e109.
[14] D. Gandla, Z. Zhuang, V.V. Jadhav, D.Q. Tan, Energy Storage Mater. 63 (2023) 102977.
[15] Z. Zhuang, B. Ju, P. Ma, L. Yang, F. Tu, Ionics 27 (2021) 1069–1079.
[16] Y. Zhao, Y. Kang, J. Wozny, et al., Nat. Rev. Mater. 8 (2023) 623–634.
[17] C. Yang, S. Xin, L. Mai, Y. You, Adv. Energy Mater. 11 (2021) 2000974.
[18] C. Vaalma, D. Buchholz, M. Weil, S. Passerini, Nat. Rev. Mater. 3 (2018) 1–11.
[19] J. Deng, W.B. Luo, S.L. Chou, H.K. Liu, S.X. Dou, Adv. Energy Mater. 8 (2018) 1701428.
[20] J.E. Zhou, R.C.K. Reddy, A. Zhong, et al., Adv. Mater. 36 (2024) 2312471.
[21] Y. Chen, X. Shi, B. Lu, J. Zhou, Adv. Energy Mater. 12 (2022) 2202851.
[22] Z. Wang, X. Feng, Y. Bai, et al., Adv. Energy Mater. 11 (2021) 2003854.
[23] M. Zhang, Y. Li, F. Wu, Y. Bai, C. Wu, Nano Energy 82 (2021) 105738.
[24] L. Wang, Z. Wei, M. Mao, et al., Energy Storage Mater. 16 (2019) 434–454.
[25] T. Wang, J. Qu, D. Legut, et al., Nano Lett. 19 (2019) 3122–3130.
[26] X. Xu, Z. Liu, S. Ji, et al., Chem. Eng. J. 359 (2019) 765–774.
[27] X. Xu, F. Li, D. Zhang, et al., Adv. Sci. 9 (2022) 2200247.
[28] M. Hu, Z. Ju, Z. Bai, et al., Small Methods 4 (2020) 1900673.
[29] B. Guo, L. Zhang, Y. Tang, J. Huang, Battery Energy 3 (2024) 20230041.
[30] X.X. Jia, X.Z. Yu, B.A. Lu, Rare Metals 40 (2021) 2455–2463.
[31] J. Ge, L. Fan, J. Wang, et al., Adv. Energy Mater. 8 (2018) 1801477.
[32] C. Wang, J. Yan, T. Li, et al., Angew. Chem. Int. Ed. 60 (2021) 25013–25019.
[33] X. Xu, J. Liu, Z. Liu, et al., Small 14 (2018) 1800793.
[34] H. Zhang, Y. Gao, X.H. Liu, et al., Adv. Funct. Mater. 32 (2022) 2107718.
[35] Q. Zhao, Y. Lu, J. Chen, Adv. Energy Mater. 7 (2017) 1601792.
[36] W. Deng, J. Chen, L. Yang, et al., Small 17 (2021) 2101058.
[37] F. Wang, F. Han, Y. He, et al., Adv. Funct. Mater. 31 (2021) 2007266.
[38] P. Ge, S. Li, L. Xu, et al., Adv. Energy Mater. 9 (2019) 1803035.
[39] Y. Qi, Y. Yang, Q. Hou, et al., Chin. Chem. Lett. 32 (2021) 1117–1120.
[40] Y. Xiao, Y. Miao, S. Wan, Y.K. Sun, S. Chen, Small 18 (2022) 2202582.
[41] X. Xu, B. Mai, Z. Liu, et al., Chem. Eng. J. 387 (2020) 124061.
[42] H. Li, H. Zhang, F. Wu, et al., Adv. Energy Mater. 12 (2022) 2202293.
[43] Y. Gong, Y. Li, Y. Li, et al., Small 19 (2023) 2206194.
[44] Y. Xiao, X. Zhao, X. Wang, et al., Adv. Energy Mater. 10 (2020) 2000666.
[45] J. Yuan, Y. Gan, X. Xu, et al., J. Colloid Interf. Sci. 626 (2022) 355–363.
[46] Y. Fang, X.Y. Yu, X.W. Lou, Adv. Mater. 30 (2018) 1706668.
[47] K. Zhu, S. Wei, Q. Zhou, et al., Nano Res. 16 (2023) 2421–2427.
[48] X. Zhu, J. Gao, J. Li, et al., Sustain. Energy Fuels 4 (2020) 2453–2461.
[49] L. Yue, D. Wang, Z. Wu, et al., Chem. Eng. J. 433 (2022) 134477.
[50] X. Ma, Y. Li, X. Long, et al., J. Energy Chem. 77 (2023) 227–238.
[51] W. Chen, M. Wu, H. Chen, L. Mo, Y. Zhu, Chin. Chem. Lett. 35 (2024) 108698.
[52] R. Jin, X. Liu, L. Yang, G. Li, S. Gao, Electrochim. Acta 259 (2018) 841–849.
[53] Q. Zhu, A. Xu, H. Chen, et al., ACS Appl. Mater. Interfaces 15 (2023) 12976–12985.
[54] H. Li, H. Zhang, M. Zarrabeitia, et al., Adv. Sustain. Syst. 6 (2022) 2200109.
[55] X. Xu, J. Liu, J. Liu, et al., Adv. Funct. Mater. 28 (2018) 1707573.
[56] H. Liu, D. Li, H. Liu, et al., Appl. Surf. Sci. 612 (2023) 155725.
[57] Y. Li, X. Sun, Z. Cheng, et al., Energy Storage Mater. 22 (2019) 275–283.
[58] L. Shao, S. Wang, J. Qi, et al., Mater. Today Phys. 19 (2021) 100422.
[59] Y. Xiao, K. Zhang, X. Zhao, et al., J. Alloy Compd. 879 (2021) 160485.
[60] D. Chao, C. Zhu, P. Yang, et al., Nat. Commun. 7 (2016) 12122.
[61] X. Xu, J. Liu, Z. Liu, et al., ACS Nano 11 (2017) 9033–9040.
[62] X. Pu, D. Zhao, C. Fu, et al., Angew. Chem. Int. Ed. 60 (2021) 21310–21318.